Understanding the effect of lattice polarisability on the electrochemical properties of lithium tetrahaloaluminates, LiAlX$_4$ (X = Cl, Br, I)

Nicolás Flores-González, Martí López, Nicolò Minafra, Jan Bohnenberger, Francesc Viñes, Svemir Rudić, Ingo Krossing, Wolfgang G. Zeier, Francesc Illas and Duncan H. Gregory*

Dr. Nicolás Flores-González, Prof. Duncan H. Gregory
School of Chemistry, Joseph Black Building
University of Glasgow
Glasgow, G12 8QQ, United Kingdom
E-mail: duncan.gregory@glasgow.ac.uk

Martí López, Dr. Francesc Viñes, Prof. Francesc Illas
Departament of Ciència de Materials i Química Física
Institut de Química Teòrica i Computacional (IQTCUB)
Universitat de Barcelona
C/Martí i Franquès 1, 08028 Barcelona, Spain

Dr. Svemir Rudić
ISIS Pulsed Neutron and Muon Source
STFC Rutherford Appleton Laboratory
Didcot, Oxfordshire, OX11 0QX, United Kingdom

Dr. Nicolò Minafra, Prof. Wolfgang G. Zeier
Institute for Inorganic and Analytical Chemistry
University of Münster
Correnstr. 39, 48149, Germany

Dr. Jan Bohnenberger, Prof. Ingo Krossing
Institut für Anorganische und Analytische Chemie
Freiburger Materialforschungszentrum (FMF)
Universität Freiburg
Albertstr. 21, 79104 Freiburg, Germany

Synthesis

Further information on the preparation of each halide is provided below:

LiAlCl$_4$: The mechanochemical approach was developed by fixing the speed to 450 rpm and gradually increased milling times from 1 to 5 h. LiAlCl$_4$, could be formed after milling for 1 h, but LiCl was also evident, suggesting that the reaction was incomplete. After 3 h, the presence of LiCl was negligible. By milling times of 5 h, diffraction peaks corresponding to LiAlCl$_4$ broadened significantly, suggesting amorphization. Optimum milling parameters of 450 rpm/3 h were adopted to achieve a crystalline, single-phase product.

LiAlBr$_4$: First attempts to make LiAlBr$_4$ *via* ball milling were performed using the same parameters employed for LiAlCl$_4$ above, but milling times needed to be increased to achieve a crystalline, single phase product. Times from 3 h to 9 h were assessed, but LiBr was consistently detected in larger quantities with increased milling time, suggesting decomposition. The rotation speed was subsequently decreased and kept constant at 300 rpm, while the milling time was gradually increased from 4 to 8 h. A milling time of 6 h was found to be optimum to deliver phase-pure LiAlBr$_4$.

LiAlI$_4$: Initially synthesis of LiAlI$_4$ *via* ball milling was performed using the experimental parameters employed in the preparation of LiAlBr$_4$ above. Milling times from 1.5 h to 6 h were explored in order to optimise the procedure. After milling for 1.5 h, a new poorly crystalline phase was observed, with neither LiI nor AlI$_3$ detected. Increasing the milling time simply led to a further decrease of crystallinity. The rotation speed was subsequently decreased from 300 to 200 rpm. The most crystalline phase-pure product was obtained by milling at 200 rpm for 6 h.

Powder X-Ray Diffraction
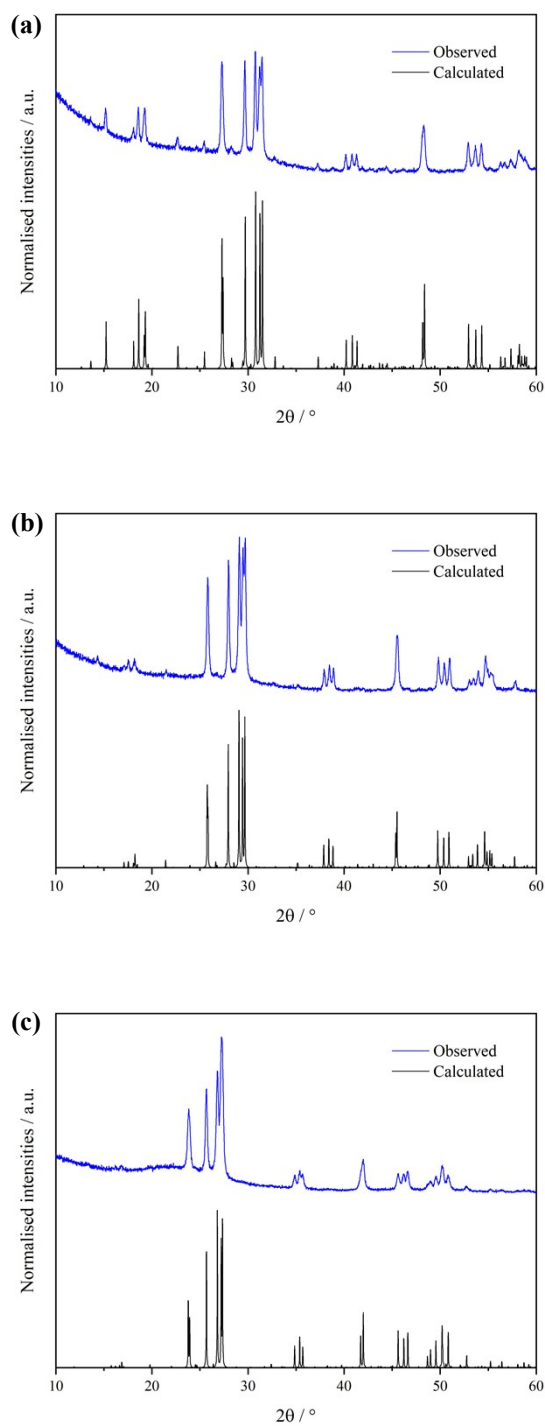
Figure S1. Room temperature PXD patterns of mechanochemically-synthesised **(a)** LiAlCl$_4$, **(b)** LiAlBr$_4$ and **(c)** LiAlI$_4$, as compared to their respective diffraction patterns simulated with data obtained from Ref.[1]

Electronic structure
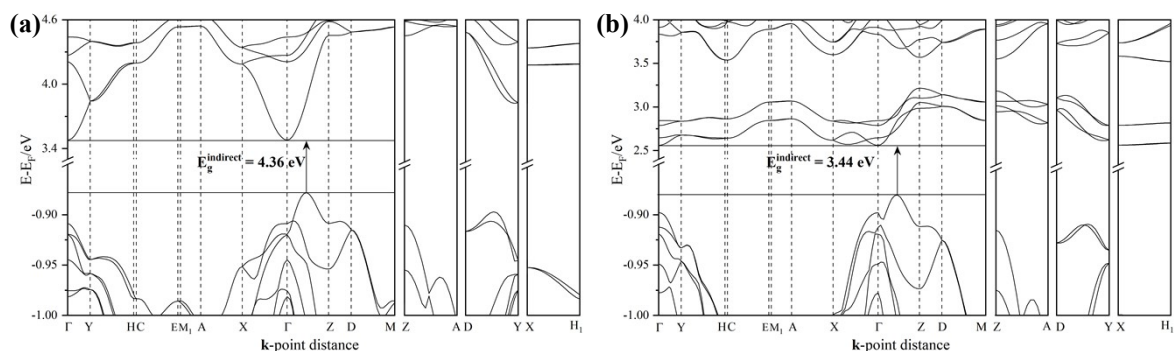
Figure S2. Computed (DFT/PBE) band structures of **(a)** LiAlBr$_4$ and **(b)** LiAlI$_4$, with band energies scaled to the Fermi level (E$_F$). High symmetry **k**-points are noted as well as the indirect gap region between the valence band maximum (VBM) and the conduction band minimum (CBM).
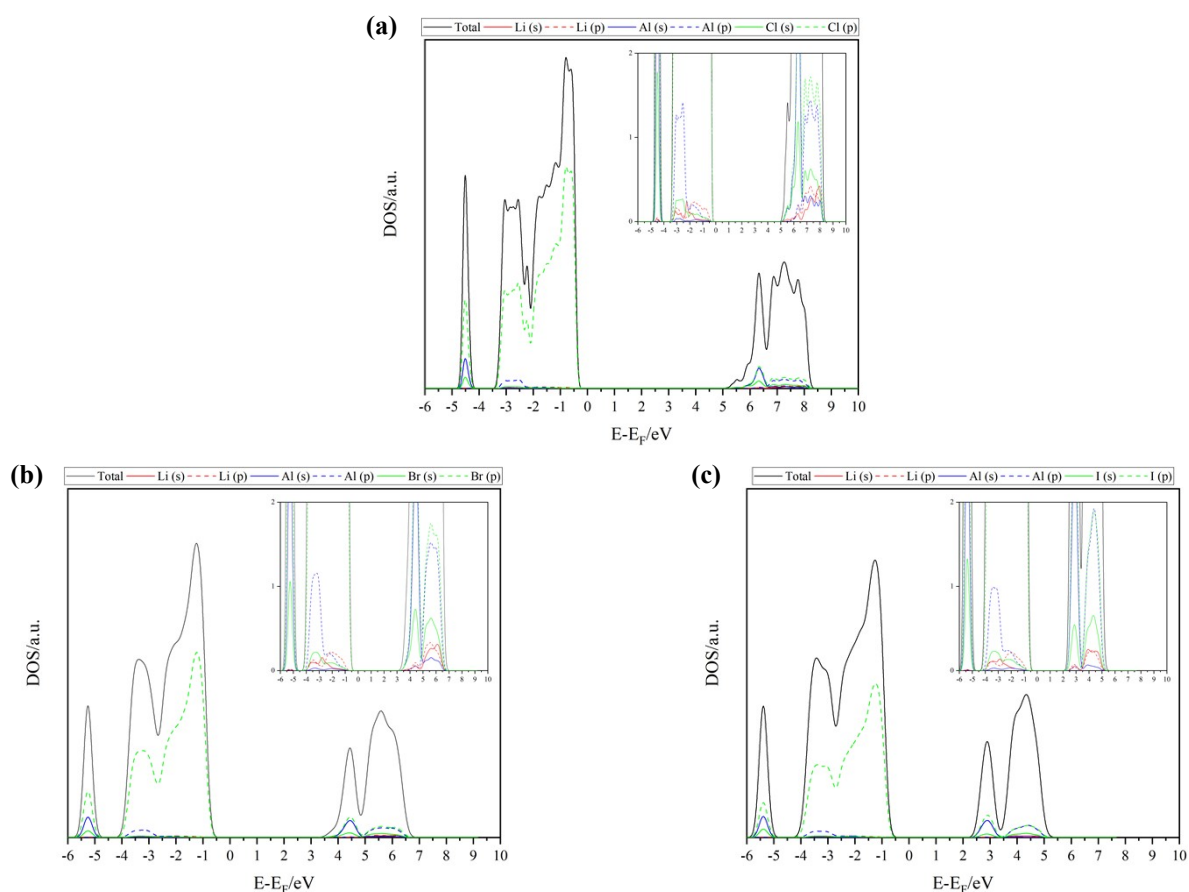

Figure S3. Computed (DFT/PBE) total and atom-projected electronic density of states (DOS) of **(a)** LiAlCl$_4$, **(b)** LiAlBr$_4$ and **(c)** LiAlI$_4$.
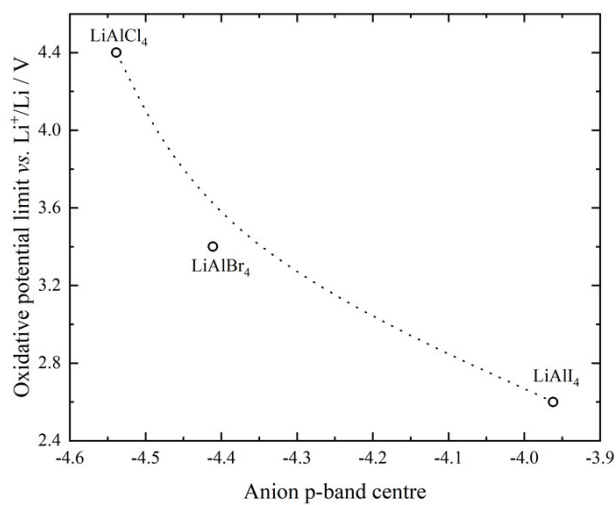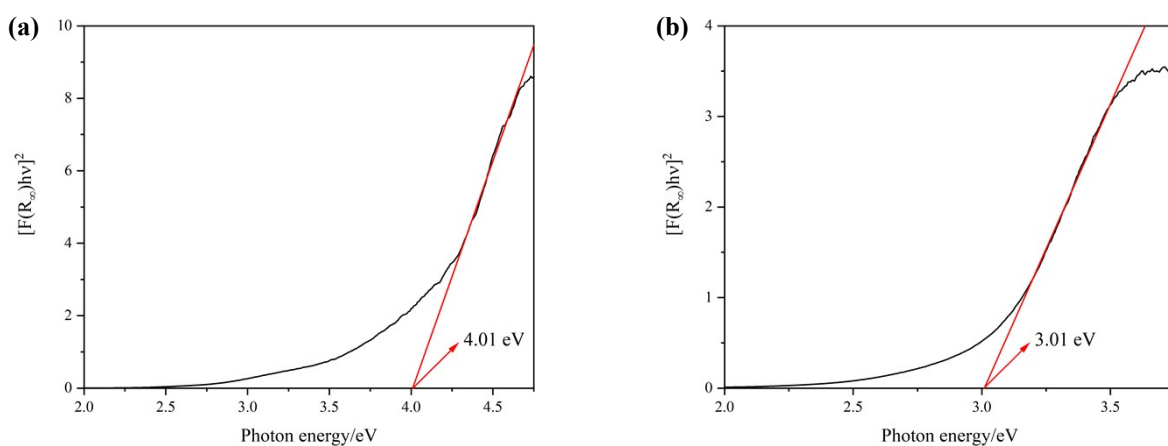
Figure S4. Correlation between the measured (by linear sweep voltammetry; LSV[1]) oxidative potential limit and computed (DFT/PBE) anion-p band centre of LiAlX_4 (X = Cl, Br, I) materials. The dotted line is a guide to the eye.
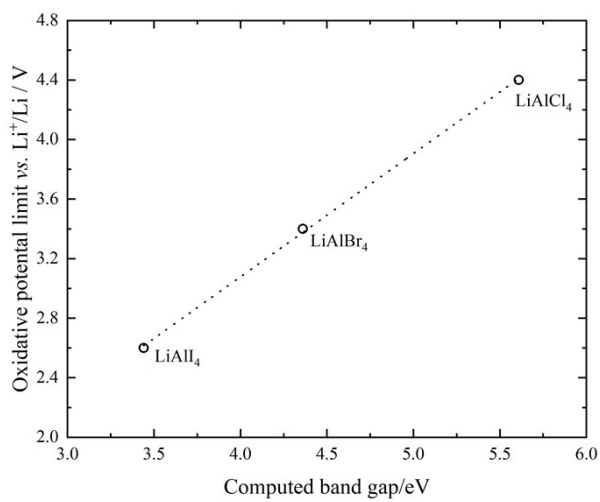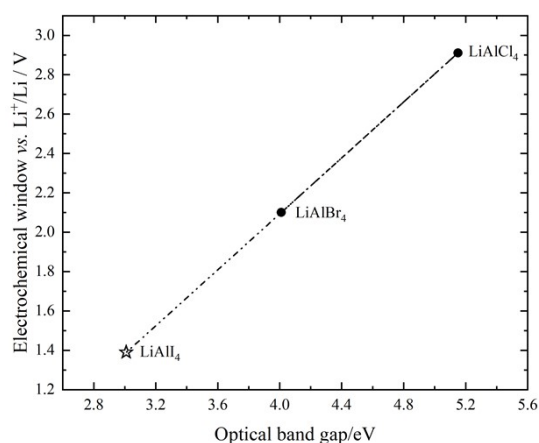

Figure S5. Correlation between the measured (LSV[1]) oxidative potential limit and the computed (DFT/PBE) band gap energies of LiAlX_4 (X = Cl, Br, I) materials. The dotted line corresponds to a linear fit (R^2 = 1.00).
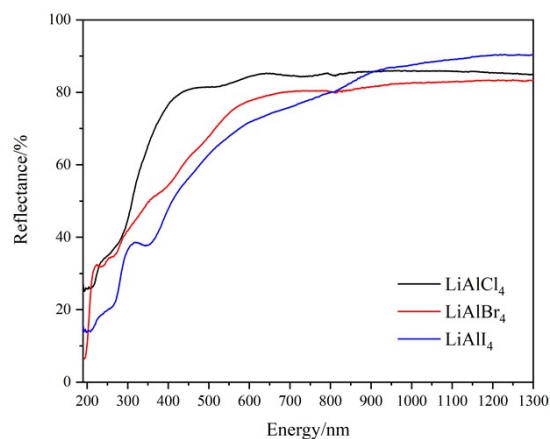
Figure S6. DR-UV-Vis spectra of LiAlX_4 materials (X = Cl, Br, I).
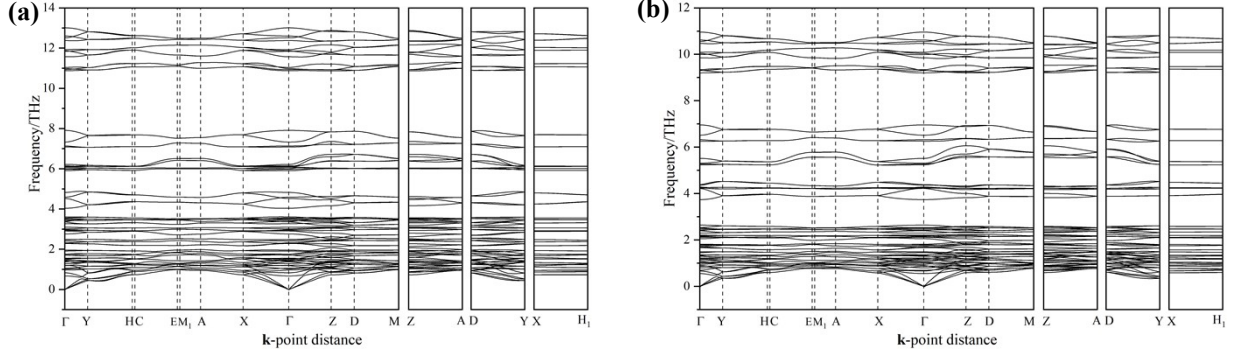

Figure S7. Tauc plots for allowed direct transitions in: **(a)** LiAlBr$_4$ and **(b)** LiAlI$_4$. The red lines correspond to the linear fits.
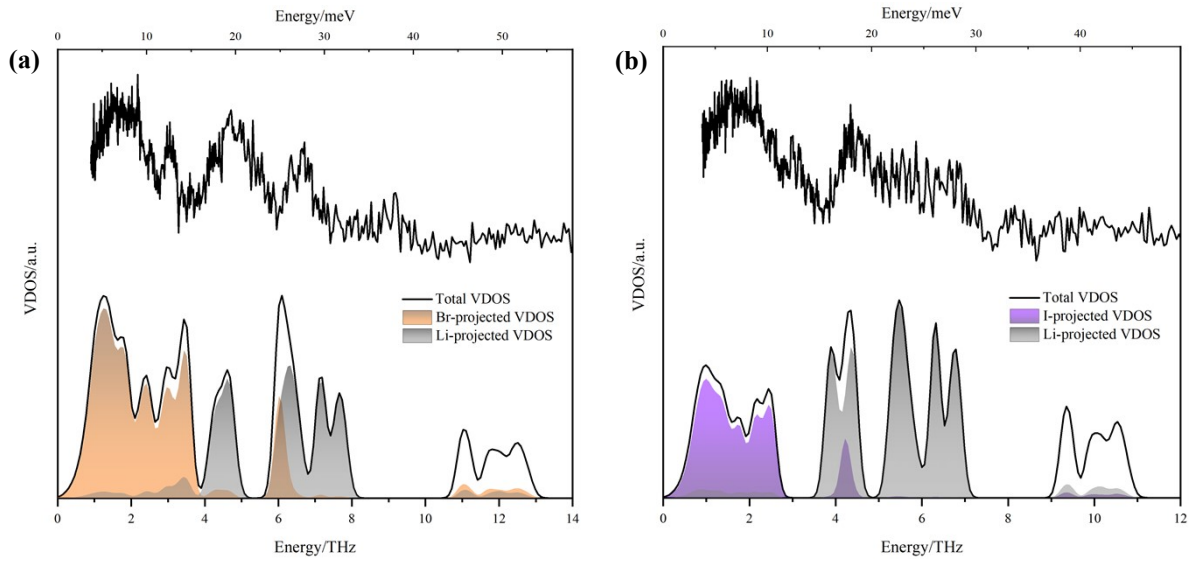

Figure S8. Correlation between computed electrochemical window (EW) values available in the literature and measured optical band gaps in LiAlX_4 (X = Cl, Br, I) materials. The EW for LiAlI$_4$ is predicted to be 1.4 V $vs.$ Li$^+$/Li.

Lattice dynamics

Figure S9. Computed (DFPT/PBE) phonon dispersions curves of **(a)** LiAlBr$_4$ and **(b)** LiAlI$_4$.

Figure S10. Comparison of computed (DFPT/PBE - Bottom) neutron-weighted VODS vs. the measured INS spectrum collected at 10 K (TOSCA, ISIS - Top) of **(a)** LiAlBr$_4$ and **(b)** LiAlI$_4$.

Table S1. Computed (DFPT/PBE average lithium-projected, anion-projected and total VDOS in LiAlX_4 (X = Cl, Br, I).

Compound	ω_{Li}			ω_X			ω_{Total}		
	THz	meV	cm^{-1}	THz	meV	cm^{-1}	THz	meV	cm^{-1}
LiAlCl$_4$	6.40	26.5	214	4.83	20.0	161	5.13	21.2	171
LiAlBr$_4$	6.03	25.0	201	2.88	11.9	96.0	4.73	19.6	158
LiAlI$_4$	5.44	22.5	182	2.04	8.44	68.1	4.86	20.1	162
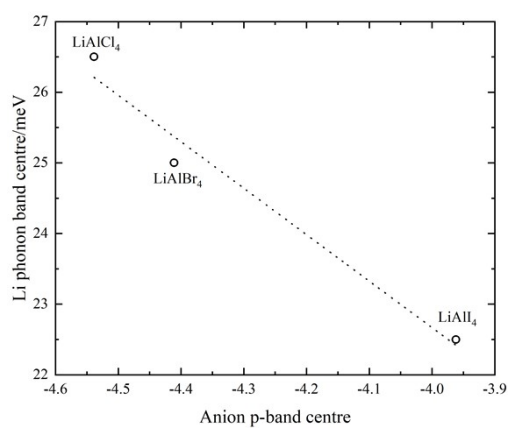
Figure S11. Correlation between computed (DFPT/PBE) Li phonon band centres and computed (DFP/PBE) anion-p band centres in LiAlX_4 materials (X = Cl, Br, I). The dotted line corresponds to a linear fit (R^2 = 0.972).
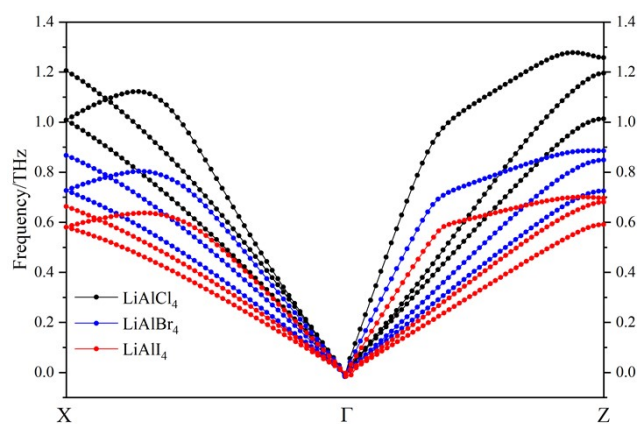
Figure S12. Example of computed (DFPT/PBE) acoustic phonon along the $\Gamma \rightarrow Z$ and $\Gamma \rightarrow X$ lines in LiAlX_4 materials (X = Cl, Br, I).

Raman spectra

An isolated $[AlX_4]^-$ ion has $3 \times 5 - 6 = 9$ normal modes of vibration which are distributed among the representations of the T_d point group according to:

$$\Gamma_{optic} = A_1(R) + E(R) + 2F_2(R) \tag{S1}$$

where A_1 is non-degenerate, E is doubly degenerate and F_2 is triply degenerate, and each term is Raman active. However, these data correspond to the gas phase and do not consider ionic interactions. This is especially true for extended ions, *e.g.* chains, layers, networks. In this work, the normal mode of vibration in crystals were obtained by nuclear site group analysis.[2] $LiAlX_4$ ($X =$ Cl, Br, I) crystallise in monoclinic space group $P2_1/c$ $\left(C_{2h}^5\right)$, with 24 atoms per unit cell. Since there are four atoms each of Li, Al, $X1$, $X2$, $X3$ $X4$ atoms that are all symmetry-equivalent, it is immediately seen by inspection of Table S2 that all atoms must occupy C_1 sites.

Table S2. Crystallographic sites in $\left(C_{2h}^5\right)$ space group.

Space group	Sites
$\left(C_{2h}^5\right)$	$eC_1(4) + (d + c + b + a)C_1(2)$

From Table S3, the vibrational modes of the crystal are then $18A_g + 18A_u + 18B_g + 18B_u$ for contribution from Li, Al, $X1$, $X2$, $X3$ and $X4$ and, therefore, the total number of optical branches are $18A_g + 17A_u + 18B_g + 16B_u$ while the acoustic branches are $A_u + 2B_u$. From Table S4, it is found that A_g and B_g modes are Raman active and A_u and B_u are infrared active. Thus, one can write:

$$\Gamma_{optic} = 18A_g(R) + 17A_u(IR) + 18B_g(R) + 16B_u(IR) \tag{S2}$$

Table S3. Irreducible representations that result from occupying each of the sites within each space group. These give the translational lattice modes.

Site	Representation
C_1	$3A_g + 3A_u + 3B_g + 3B_u$
C_i	$3A_u + 3B_u$
C_2	$A_g + A_u + 2B_g + 2B_u$
C_s	$2A_g + A_u + B_g + 2B_u$
C_{2h}	$A_u + 2B_u$

C_{2h}	E	C_2^z	i	σ_h	Selections rules	
A_g	1	1	1	1	R_z	$\alpha_{xx}, \alpha_{yy}, \alpha_{zz}, \alpha_{xy}$
A_u	1	1	-1	-1	T_z	
B_g	1	-1	1	-1	R_x, R_y	α_{xz}, α_{yz}
B_u	1	-1	-1	1	T_x, T_y	

The external and internal vibrational modes can be obtained by treating the tetrahaloaluminate anion independently. In other words, one can consider a unit cell built up from two species in each formula unit, *i.e.* a lithium cation and a $[AlX_4]^-$ anion. Each must occupy C_1 sites, and from Table S3 this gives $6A_g + 6A_u + 6B_g + 6B_u$ modes. $A_u + 2B_u$. are acoustical modes so there remain $6A_g + 5A_u + 6B_g + 4B_u$ modes, which are optical modes of translational character.

From Table S5, $3A_g + 3A_u + 3B_g + 3B_u$ may be assigned as librational modes resulting from oscillations of the tetrachloroaluminate anion. No librational modes are assigned to the Li^+ cation since it has no rotational degrees of freedom. It should be noted that since A_g, A_u, B_g and B_u modes arise from both translational and rotational motions, they may not be assigned as pure librational or pure translational modes. Summing up, the total number of external modes of $LiAlX_4$ are thus $9A_g + 8A_u + 9B_g + 7B_u$. By subtracting the external modes from the total number of modes (Γ_{optic}), one obtains the result that the internal vibrational modes are $9A_g + 9A_u + 9B_g + 9B_u$.

Table S5. Librational lattice modes of polyatomic units when placed on each of the possible sites in the unit cell.

Site	Representation
C_1	$3A_g + 3A_u + 3B_g + 3B_u$
C_i	$3A_g + 3B_g$
C_2	$A_g + A_u + 2B_g + 2B_u$
C_s	$A_g + 2A_u + 2B_g + B_u$
C_{2h}	$A_g + 2B_g$

Computationally, to obtain a Raman spectrum from an optimised crystal structure, one needs to compute: (1) the phonons at the Γ point, *i.e.* the Brillouin zone centre, and (2) the derivative of the polarisability, *i.e.* the macroscopic dielectric tensor[3]. The former gives the vibrational mode frequency and it can be calculated either *via* the finite-displacement (FD) or density-functional perturbation theory (DFPT) approach implemented in VASP. The latter macroscopic dielectric tensor can be obtained *via* Equations S3-S5 already coded in Ref.[4]

$$I_{Raman} = 45\alpha^2 + 7\beta^2 \tag{S3}$$

$$\alpha = \frac{1}{3}\left(\alpha_{xx} + \alpha_{yy} + \alpha_{zz}\right) \tag{S4}$$

$$\beta = \frac{1}{2}\left[\left(\alpha_{xx} - \alpha_{yy}\right)^2 + \left(\alpha_{xx} - \alpha_{zz}\right)^2 + \left(\alpha_{yy} - \alpha_{zz}\right)^2 + 6\left(\alpha_{xy}^2 + \alpha_{xz}^2 + \alpha_{yz}^2\right)\right] \tag{S5}$$
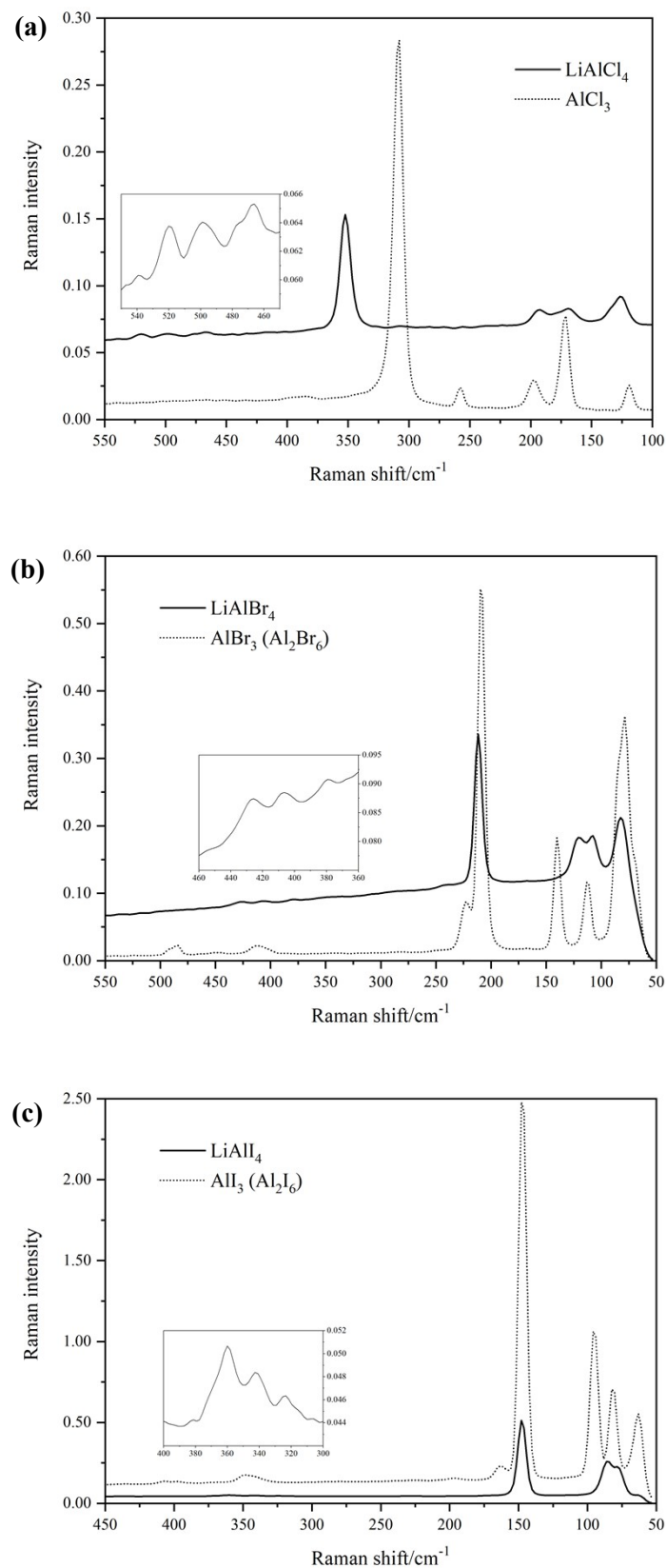
where α is the mean polarisability derivative and β is the anisotropy of the polarisability tensor derivative. Once the band positions and intensities have been calculated, the spectrum is then fitted by a Gaussian function, already coded in Ref.[4]

Tables S6. Experimental and computed Raman (DFT/FD/PBE) frequencies of LiAlX_4 (X = Cl, Br I).

λ_{laser} = 1064 nm.

| LiAlCl$_4$			LiAlBr$_4$			LiAlI$_4$		
Experiment ω/cm^{-1}	FD/PBE ω/cm^{-1}	Mode	Experiment ω/cm^{-1}	FD/PBE ω/cm^{-1}	Mode	Experiment ω/cm^{-1}	FD/PBE ω/cm^{-1}	Mode
	523.4	B_g		428.4	B_g		360.8	B_g
520	519.5	A_g	426	425.6	A_g	360	358.6	A_g
499	496.1	B_g	406	403.5	B_g	343	341.2	B_g
	494.8	A_g		402.6	A_g		339.5	A_g
466	461.3	A_g	379	373.5	A_g	324	316.6	A_g
	459.8	B_g		369.9	B_g		312.7	B_g
352	344.9	A_g		241.4	A_g		214.1	A_g
	343.9	B_g		239.6	B_g		212.1	B_g
	268.9	B_g		210.5	B_g		186.8	B_g
	267.8	A_g	212	207.9	A_g		179.7	A_g
	247.5	B_g		206.2	B_g		145.4	B_g
	246.8	A_g		203.5	A_g	148	144.8	A_g
	202.7	B_g		163.1	B_g		143.5	B_g
192	195.8	A_g		136.6	A_g		127.2	A_g
	191.5	B_g		122.6	B_g		89.8	B_g
	179.1	A_g		119.5	B_g	86	85.9	A_g
	171.6	B_g	121	117.9	A_g		84.3	B_g
169	163.3	B_g		113.9	A_g		81.8	A_g
	162.5	A_g		105.0	B_g	79	75.0	B_g
	145.0	A_g		102.2	A_g		74.2	A_g
	133.2	B_g		84.2	A_g		61.6	A_g
127	124.9	B_g		83.8	B_g		59.9	B_g
	122.8	A_g		78.6	B_g		58.1	B_g
	118.3	A_g		77.6	A_g		56.6	A_g
	98.5	B_g		66.4	B_g		50.5	B_g
	92.3	A_g		64.7	A_g		49.3	A_g
	85.7	A_g		58.4	B_g		45.7	B_g
	83.1	B_g		57.8	A_g		44.0	A_g
	74.3	B_g		51.5	B_g		40.8	B_g
	74.0	A_g		50.3	A_g		39.5	A_g
	67.7	A_g		48.9	B_g		38.6	B_g
	64.6	B_g		46.5	A_g		35.4	A_g
	56.5	B_g		40.3	B_g		32.1	B_g
	50.9	A_g		35.8	A_g		29.8	A_g
	50.3	B_g		34.5	B_g		27.2	B_g
	32.0	A_g		22.6	A_g		18.9	A_g

Figure S13. Theoretical simulated (DFT/FD/PBE) Raman spectrum of LiAlCl$_4$ showing the underlying 36 Raman active modes.

Figure S14. (a) Theoretically simulated (DFT/FD/PBE) vs. experimentally observed Raman spectrum of LiAlBr$_4$

(λ_{laser} = 1064 nm). **(b)** Theoretical simulated (DFT/FD/PBE) Raman spectrum of LiAlBr$_4$ showing the underlying 36 Raman active modes.

Figure S15. (a) Theoretically simulated (DFT/FD/PBE) vs. experimentally observed Raman spectrum of LiAlI$_4$ (λ_{laser} = 1064 nm). **(b)** Theoretical simulated (DFT/FD/PBE) Raman spectrum of LiAlI$_4$ showing the underlying 36 Raman active modes.

Figure S16. Comparison of experimental room temperature Raman spectra of LiAlX_4 vs. AlX_3 starting materials. **(a)** X = Cl, **(b)** X = Br, and **(c)** X = I (λ_{laser} = 1064 nm).
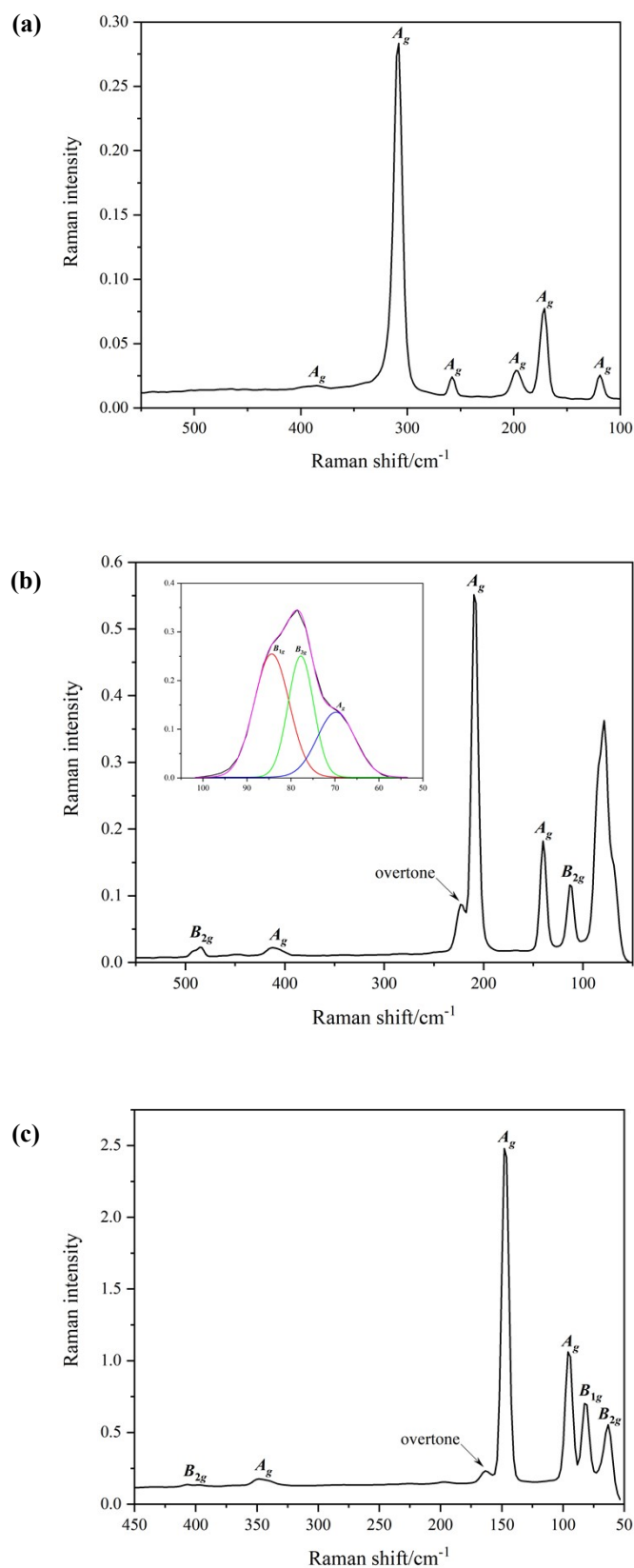
Figure S17. Room temperature Raman spectra of (a) AlCl$_3$, (b) AlBr$_3$ and (c) AlI$_3$, showing the assignment of their respective bands (λ_{laser} = 1064 nm).

Table S7. Assignment of the Raman wave numbers (in cm^{-1}) for AlX_3 (X = Cl, Br, I).[5-7]

AlCl$_3$	Assignment	AlBr$_3$(Al$_2$Br$_6$)	Assignment	AlI$_3$(Al$_2$I$_6$)	Assignment
385	A_g	486	B_{2g}	406	B_{2g}
308	A_g	412	A_g	349	A_g
258	A_g	233	*overtone*	163	*overtone*
198	A_g	210	A_g	148	A_g
171	A_g	140	A_g	96	A_g
119	A_g	113	B_{2g}	82	B_{1g}
		84[a]	B_{1g}	63	B_{2g}
		78[a]	B_{3g}		
		70[a]	A_g		

(a) deconvoluted values
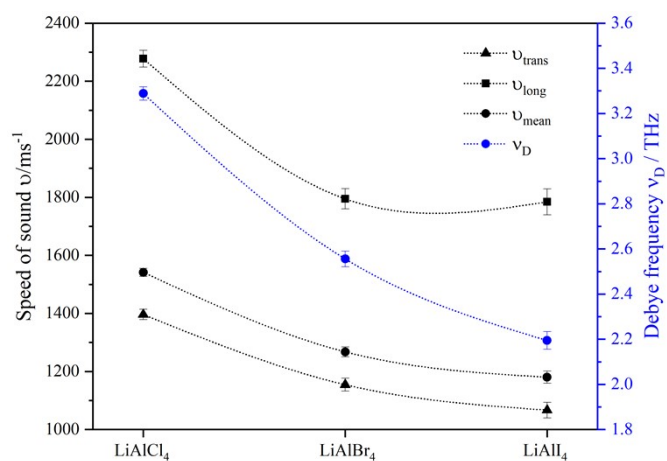
Figure S18. Measured longitudinal, transverse and mean speeds of sound in LiAlX_4 materials (X = Cl, Br, I) and their extracted Debye frequencies.
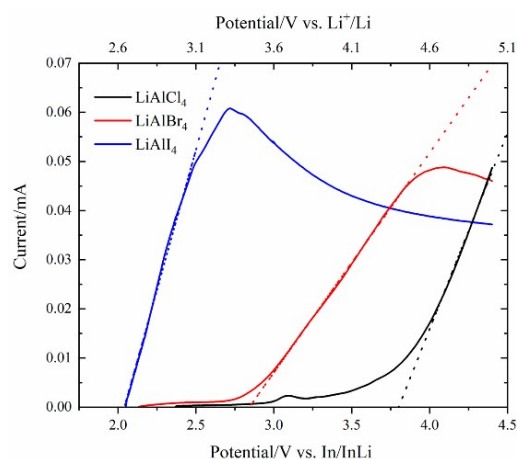
Figure S19. Room temperature linear sweep voltammogram (0.1 mV s^{-1}) of InLi|LiAlX_4|LiAlX_4 + C cells. Dashed lines indicate linear fits of the faradaic region. The bottom *x*-axis shows the values of the voltage versus In/InLi, the top *x*-axis shows the corresponding values of voltage versus Li$^+$/Li.[1] Further permission related to the material excerpted should be directed to the ACS. https://pubs.acs.org/doi/10.1021/acsmaterialslett.1c00055.

Table S8. Transport data of mechanochemically-synthesised LiAlX_4 (X = Cl, Br, I) materials.[1]

Material	$\sigma_{RT} \times 10^5$ / S cm^{-1}	$\sigma_0 \times 10^{-5}$ / K S cm^{-1}	E$_a$ / eV
LiAlCl$_4$	2.9(2)	8.6(7)	0.473(2)
LiAlBr$_4$	3.3(2)	2.5(4)	0.437(4)
LiAlI$_4$	1.2(1)	0.61(7)	0.429(3)

References

1. N. Flores-González, N. Minafra, G. Dewald, H. Reardon, R. I. Smith, S. Adams, W. G. Zeier and D. H. Gregory, *ACS Materials Lett.*, 2021, **3**, 652-657.
2. D. L. Rousseau, R. P. Bauman and S. P. S. Porto, *J. Raman Spectrosc.*, 1981, **10**, 253-290.
3. D. Porezag and M. R. Pederson, *Phys. Rev. B*, 1996, **54**, 7830-7836.
4. A. Fonari and S. Stauffer, vasp_raman_py, https://github.com/raman-sc/VASP/.
5. J. A. Sanjurjo, M. A. Pires, G. E. Barberis, C. Rettori and Y. Yacoby, *Molecular Crystals and Liquid Crystals Science and Technology. Section A. Molecular Crystals and Liquid Crystals*, 1994, **244**, 287-292.
6. G. M. Begun, C. R. Boston, G. Torsi and G. Mamantov, *Inorg. Chem.*, 1971, **10**, 886-889.
7. I. R. Beattie, T. Gilson and G. A. Ozin, *J. Chem. Soc. A*, 1968, 813-815.